



Multifunctional iron-biochar composites for the removal of potentially toxic elements, inherent cations, and hetero-chloride from hydraulic fracturing wastewater



Yuqing Sun^{a,b}, Iris K.M. Yu^a, Daniel C.W. Tsang^{a,*}, Xinde Cao^c, Daohui Lin^d, Linling Wang^e, Nigel J.D. Graham^f, Daniel S. Alessi^g, Michael Komárek^h, Yong Sik Ok^{i,*}, Yujie Feng^b, Xiang-Dong Li^a

^a Department of Civil and Environmental Engineering, Hong Kong Polytechnic University, Hung Hom, Kowloon, Hong Kong, China

^b State Key Laboratory of Urban Water Resource and Environment, Harbin Institute of Technology, Harbin 150090, China

^c School of Environmental Science and Engineering, Shanghai Jiao Tong University, 800 Dongchuan Road, Shanghai 200240, China

^d Department of Environmental Science, Zhejiang University, Hangzhou 310058, China

^e School of Environmental Science and Engineering, Huazhong University of Science and Technology, Wuhan 430074, China

^f Environmental and Water Resources Engineering, Department of Civil and Environmental Engineering, Imperial College London, South Kensington, London SW7 2AZ, UK

^g Department of Earth and Atmospheric Sciences, University of Alberta, Edmonton, Alberta T6G 2E3, Canada

^h Faculty of Environmental Sciences, Czech University of Life Sciences, Kamýcká 129, 165 00 Prague-Suchbát, Czech Republic

ⁱ Korea Biochar Research Center, O-Jeong Eco-Resilience Institute (OJERI), Division of Environmental Science and Ecological Engineering, Korea University, Seoul 02841, Republic of Korea

ARTICLE INFO

Keywords:

Engineered biochar
Mineral-carbon composites
Metals/metalloids
Fracturing wastewater treatment
Sustainable remediation

ABSTRACT

This paper evaluates a novel sorbent for the removal of potentially toxic elements, inherent cations, and hetero-chloride from hydraulic fracturing wastewater (FWW). A series of iron-biochar (Fe-BC) composites with different Fe/BC impregnation mass ratios (0.5:1, 1:1, and 2:1) were prepared by mixing forestry wood waste-derived BC powder with an aqueous FeCl₃ solution and subsequently pyrolyzing them at 1000 °C in a N₂-purged tubular furnace. The porosity, surface morphology, crystalline structure, and interfacial chemical behavior of the Fe-BC composites were characterized, revealing that Fe chelated with C–O bonds as C–O–Fe moieties on the BC surface, which were subsequently reduced to a C=C bond and nanoscale zerovalent Fe (nZVI) during pyrolysis. The performance of the Fe-BC composites was evaluated for simultaneous removal of potentially toxic elements (Cu(II), Cr(VI), Zn(II), and As(V)), inherent cations (K, Na, Ca, Mg, Ba, and Sr), hetero-chloride (1,1,2-trichloroethane (1,1,2-TCA)), and total organic carbon (TOC) from high-salinity (233 g L⁻¹ total dissolved solids (TDS)) model FWW. By elucidating the removal mechanisms of different contaminants, we demonstrated that Fe-BC (1:1) had an optimal reducing/charge-transfer reactivity owing to the homogenous distribution of nZVI with the highest Fe⁰/Fe²⁺ ratio. A lower Fe content in Fe-BC (0.5:1) resulted in a rapid exhaustion of Fe⁰, while a higher Fe content in Fe-BC (2:1) caused severe aggregation and oxidation of Fe⁰, contributing to its complexation/(co-)precipitation with Fe²⁺/Fe³⁺. All of the synthesized Fe-BC composites exhibited a high removal capacity for inherent cations (3.2–7.2 g g⁻¹) in FWW through bridging with the C–O bonds and cation-π interactions. Overall, this study illustrated the potential efficacy and mechanistic roles of Fe-BC composites for (pre-)treatment of high-salinity and complex FWW.

1. Introduction

Significant increase in hydraulic fracturing has been forecasted in the future (e.g., ~45% in 2013–2040 for the US and 8–12% in 2015–2020 for China) due to the reduced cost of harvesting gas and oil from shale formations, for moderating the rising global demand for

energy from conventional sources (Abass et al., 2017). This leads to the generation of large amounts of fracturing wastewater (FWW) as a primary negative environmental impact. FWW contains high levels of total dissolved solids (TDS), potentially toxic elements, poorly biodegradable hetero-chlorides, and other dissolved organic substances (Abualfaraj et al., 2014; Shih et al., 2015), which may exert detrimental impacts on

* Corresponding authors.

E-mail addresses: dan.tsang@polyu.edu.hk (D.C.W. Tsang), yongsikok@korea.ac.kr (Y.S. Ok).

<https://doi.org/10.1016/j.envint.2019.01.047>

Received 25 October 2018; Received in revised form 17 January 2019; Accepted 17 January 2019

Available online 24 January 2019

0160-4120/ © 2019 The Authors. Published by Elsevier Ltd. This is an open access article under the CC BY-NC-ND license

(<http://creativecommons.org/licenses/by-nc-nd/4.0/>).

reproduction and mortality in organisms (Blewett et al., 2017). FWW management strategies favor its treatment, recycling, and reuse or discharge because of both the cost and lack of deep injection wells, and legislative and social license constraints (Butkovskiy et al., 2017). Among new technologies (e.g., electrocoagulation (Kausley et al., 2017), advanced oxidation (Abass et al., 2017), and microbial fuel cells (Shrestha et al., 2018)) which have yet to be proven at full scale, reverse osmosis (RO) has been considered the most widely applicable treatment method to remove over 70% of the inorganic (Shaffer et al., 2013) and most of the organic compounds of concern in FWW, except low-molecular-weight chlorinated hydrocarbons (Butkovskiy et al., 2017). However, RO is susceptible to scaling and bio-fouling, which should be prevented by prior removal of minerals and organics via extensive pretreatments, e.g., microfiltration, biological, and adsorption-based treatment (Camarillo et al., 2016). The latter, in particular, can also reduce salinity and remove potentially toxic elements and poorly biodegradable hetero-chlorides, which allow for the application of downstream biological treatments.

Our previous studies have demonstrated granular or nanoscale zero-valent iron (ZVI) as a suitable sorbent, with high reactivity in terms of chemical reduction, complexation, and (co-)precipitation, for the removal of multiple inorganic and organic contaminants which are typically present in FWW (Lei et al., 2018a; Sun et al., 2017a, 2017b, 2018). In these studies, the use of a protective polymer-based coating could prevent agglomeration of nanoscale ZVI (nZVI) particles, which improved their reactivity (Lei et al., 2018a; Sun et al., 2017b). However, long-term resistance against passivation in high-salinity FWW remains a challenge in sustaining a high level of performance of nZVI (Lei et al., 2018a; Sun et al., 2018).

Recently, porous carbon or mineral materials (e.g., activated carbon and zeolite) have attracted much attention as nZVI supporters, owing to their high surface area and specific pore/channel structure that prevent oxidation and aggregation of nZVI (Stefaniuk et al., 2016), and therefore may be applicable for FWW treatment (Butkovskiy et al., 2018; Chang et al., 2017; Lobo et al., 2016). Compared to activated carbon, biochar (BC), a porous material derived from biological waste via pyrolysis, offers a more sustainable option as a solid support for nZVI (Rajapaksha et al., 2016). More importantly, BC may carry more abundant oxygen-containing surface functional groups (e.g., C–O, C–O–C, and C=O) than activated carbon, which may be capable of interacting with Fe to form multifunctional Fe-BC composites (Zhu et al., 2017).

The synthesis of Fe-BC composites, for example, through a one-step pyrolysis of BC pretreated with FeCl₃ at high temperature (i.e., 1000 °C; Lawrinenko et al., 2016; Wu et al., 2015), enables the complimentary coupling of the respective adsorptive, reductive, and complexing capacities of BC and Fe in one composite material. We herein adopt the lignin-containing wood waste as the feedstock, which results in macro- and meso-porous structure for harboring nZVI. The technique tends to be more economic, scalable, and sustainable for engineering applications than other sorbents (Lawrinenko et al., 2016; Rajapaksha et al., 2016). Despite the advantages of Fe-BC composites in terms of magnetization, high specific surface area, high reactivity, etc., their applications in wastewater or soil remediation have been limited to the removal of chlorinated organics (e.g., 2,4-dichlorophenol and 1,1,1-trichloroethane) and potentially toxic elements (e.g., Cu, Zn, Pb, Ni, Cd, As, Cr, and Ag) in low ionic strength systems (Dong et al., 2017; Li et al., 2017; Oh et al., 2016; Wang et al., 2017a; Zhou et al., 2014; Zhu et al., 2017). Therefore, it is uncertain that if Fe-BC composites are capable to simultaneously remove multiple contaminants in high-salinity FWW. Moreover, the relationships between the physicochemical structural properties, performance, and mechanisms are not well understood, which are critical knowledge gaps in designing advanced biochar-based materials for environmental remediation. Furthermore, the impact of a high-salinity background on the Fe-BC performance is yet to be revealed, which is a critical challenge in FWW treatment.

Table 1
Chemical compositions of Day-90 hydraulic fracturing wastewater (Day-90 FWW).

Composition	Day-90 FWW	Unit
Potassium	16,704	mg L ⁻¹
Calcium	21,160	mg L ⁻¹
Sodium	44,040	mg L ⁻¹
Barium	2130	mg L ⁻¹
Magnesium	1679	mg L ⁻¹
Strontium (II)	3154	mg L ⁻¹
Iron (III)	117	mg L ⁻¹
Chloride	127,018	mg L ⁻¹
Nitrate	1085	mg L ⁻¹
Bromide	1175	mg L ⁻¹
Boron	18.1	mg L ⁻¹
Copper (II)	116	mg L ⁻¹
Zinc (II)	247	mg L ⁻¹
Chromium (VI)	2.2	mg L ⁻¹
Arsenic (V)	1.1	mg L ⁻¹
1,1,2-Trichloroethane	2.0	mg L ⁻¹
pH	5.9	–
TDS	233.3	g L ⁻¹
TOC ^a	670	mg L ⁻¹

^a TOC mainly derived from polyacrylamide (0.088%, v/v), ethylene glycol (0.043%, v/v), and glutaraldehyde (0.010%, v/v), which were organic compounds commonly found in FWW.

In this study, Fe-BC composites with different Fe/BC impregnation mass ratios (0.5:1, 1:1, and 2:1) were synthesized through a one-step pyrolysis of FeCl₃-pretreated BC at 1000 °C with continuous N₂ purging. The objectives of this research were to: (i) determine the impact of the Fe/BC mass ratio on the physicochemical properties, surface structure, and interfacial chemical behavior of the resulting Fe-BC composites; and (ii) to identify the diverse mechanisms for the removal of potentially toxic elements (Cu(II), Cr(VI), Zn(II), and As(V)), inherent cations (Na, Ca, K, Mg, Sr, and Ba), 1,1,2-TCA, and TOC from high-salinity FWW by Fe-BC composites. The results of this study should be conducive to improving future design of high-performance, engineered Fe-BC composites for full-scale, practical FWW (pre-)treatment.

2. Materials and methods

2.1. Chemical composition of synthetic FWW

Model Day-90 FWW (representing the fluids returning to the ground surface 90 days after well creation) was prepared according to “Sampling and Analysis of Water Streams Associated with the Development of Marcellus Shale Gas” (Hayes, 2009) (Table 1), as used in previous studies (Chen et al., 2016, 2017; Lei et al., 2018a; Sun et al., 2017a, 2017b, 2018). Detailed information on the chemical composition is shown in the Supporting information. The metal speciation in Day-90 FWW was calculated using Visual MINTEQ version 3.0 (Tables S1 and S2 in the Supporting information).

2.2. Preparation of Fe-BC composites

The BC derived from forestry wood waste (*Acacia confusa* and *Celtis sinensis*) was supplied by Kadoorie Farm and Botanic Garden (KFBG) in Hong Kong, where slow pyrolysis (at 5 °C min⁻¹) at 650 °C for at least 15 h was performed to produce biochars for forestry/agricultural use at KFBG. The as-received BC was ground and sieved to be within the size range of 0.075–1.18 mm before use. The Fe-BC composites were prepared according to a method developed in previous studies (Lawrinenko et al., 2016; Zhu et al., 2017). Detailed information on the synthesis process is available in the Supporting information. The obtained products are denoted as Fe-BC (0.5:1), Fe-BC (1:1), and Fe-BC (2:1), respectively, where the suffix number represents the Fe/BC

impregnation mass ratios.

2.3. Microscopic characterization of Fe-BC composites

The characteristics of the BC and the Fe-BC composites were identified via employing the Brunauer-Emmett-Teller (BET) surface area and porosity, scanning electron microscopy-energy dispersive X-ray spectroscopy (SEM-EDX), X-ray diffraction (XRD), Raman spectroscopy, Fourier transform infrared spectroscopy (FTIR), thermogravimetric analysis (TGA), and X-ray photoelectron spectroscopy (XPS) analyses. Detailed information on the characterization is available in the Supporting information.

2.4. Treatment of Day-90 FWW by Fe-BC composites

To investigate the removal kinetics of Cu(II), Cr(VI), Zn(II), As(V), and 1,1,2-TCA from Day-90 FWW by Fe-BC composites with different Fe/BC impregnation mass ratios (0.5:1, 1:1, and 2:1), 2 g L⁻¹ suspensions of Fe-BC composites (determined according to our previous work; Lei et al., 2018a; Sun et al., 2017a, 2017b, 2018) were reacted with 25-mL Day-90 FWW, while a similar reaction with BC was conducted for comparison in 60-mL glass vials with triple-sealed closures. Detailed information on the treatment of Day-90 FWW is available in the Supporting information.

2.5. Analytical methods

The samples were analyzed for As(V) by atomic absorption spectrometry (AAS) using a vapor generation accessory (VGA-AAS, Agilent VGA77, limit of detection (LOD) of 1 μg L⁻¹) and inductively coupled plasma-atomic emission spectrometry (ICP-AES, Spectro Arcos) for Zn, Fe, Na, Ca, K, Mg, Sr, and Ba (LOD of 0.1 mg L⁻¹), after total digestion in HNO₃ and HClO₄. Cr(VI) and Cu(II) concentrations were determined by UV-Vis spectrophotometry (US EPA Clean Water Act Analytical Methods, 3500-B-2009). GC-MS (Agilent 7890B GC analyzer, 5977 Mass Selective Detector, USA) was used to measure concentrations of 1,1,2-TCA subsequent to the hexane extraction procedure. Detailed information on the GC-MS setup is available in the Supporting information. The TOC was measured using a TOC analyzer (SSM-5000A, Shimadzu, Japan, LOD of 0.1 mg L⁻¹).

Calibration of standard organic/inorganic concentrations was carried out prior to each analysis. Standards were analyzed every 10 samples for quality assurance and quality control. All experiments were performed in duplicate (or triplicate when deviation was > 5%), and the results are presented as mean ± deviations. One-way analysis of variance (ANOVA) followed by the Duncan test was applied to analyze the significance of the difference between data (SPSS version 22.0). The lower-case letters in Figs. 4, 5, 7, and S6 indicate the significance level (p < 0.05) in the results.

3. Results and discussion

3.1. Physicochemical properties and crystalline structure of Fe-BC composites

Selected physicochemical properties of BC and the synthesized Fe-BC composites with impregnation of different Fe/BC mass ratios (0.5:1, 1:1, and 2:1) are summarized in Table 2. The Fe content in the Fe-BC composites ranged from 26.2 ± 0.1 to 54.2 ± 2.7 wt%, lower than the 33.3–66.6% Fe present in the Fe/BC mass ratios upon initial mixing. This loss of Fe was associated with washing steps that removed excess Fe. Meanwhile, the contents of Ca, K, and Mg markedly decreased after Fe addition and washing. Notably, the increases in molar concentration of loaded Fe (from 0.02 to 4.7–9.7 mol kg⁻¹) were higher than the losses of Ca (from 0.47 to 0.32–0.20 mol kg⁻¹), K (from 0.12 to 0.038–0.018 mol kg⁻¹), and Mg (from 0.029 to 0.015–0.004 mol kg⁻¹)

from the Fe-BC composites (0.5:1–2:1). These results suggest that Fe was loaded on the BC surface firstly through competitive ion exchange and then by precipitation after saturation of exchangeable sites that originally held Ca, Mg, and K (Li et al., 2017).

The specific surface area decreased from 227.3 m² g⁻¹ for the control BC to 223.0–138.4 m² g⁻¹ for the Fe-BC composites, which might have been caused by blockage of pores on the BC surface after Fe precipitation. Moreover, the pre-soaking in a highly acidic FeCl₃ solution, at pH = 0.8–1.8, may have eroded the carbon structure during pyrolysis, resulting in fewer micropores (from 74.2 to 73.2–51.6% of total pore volume) and larger pore diameters (from 2.34 to 2.39–3.01 nm) in the Fe-BC composites (Wang et al., 2017b). Compared with the control BC, the pH of the Fe-BC composites decreased from 9.7 to 5.6–5.2, which could be attributed to the hydrolysis of Fe²⁺/Fe³⁺, viz: (i) 4Fe²⁺ + O₂ + 4.5H₂O → 2Fe₂O₃·0.5H₂O + 8H⁺, (ii) 6Fe²⁺ + O₂ + 6H₂O → 2Fe₃O₄ + 12H⁺, and (iii) Fe³⁺ + H₂O → Fe(OH)²⁺ + H⁺ (Zhang et al., 2017). The zeta potential of Fe-BC composites (from -36.1 to 14.1–26.0 mV) and the pH value at the point of zero charge (pH_{pzc}) (from 4.9 to 5.4–5.6) increased owing to an increasingly positive surface charge after the formation of various iron (hydr)oxides minerals with higher Fe mass ratios. Thus, Fe impregnation can reduce the inherent alkalinity of BC, and thereby significantly increase the BC adsorption capacity for removing oxyanions (e.g., Cr(VI) and As(V)) through electrostatic interaction with the more positively charged BC surface (Cho et al., 2017a). The cation exchange capacity (CEC) of Fe-BC composites was also found to decrease (from 975 to 781–553 meq kg⁻¹) in accordance with the lower contents of Ca, K, and Mg, or blockage of exchangeable sites due to Fe precipitation.

The SEM-EDX analysis of the BC and Fe-BC composites are presented in Fig. S1. In contrast to the smooth surface with distinct channels and internal micropores on the control BC (Fig. S1a), large numbers of Fe particles were observed on the surface of Fe-BC composites. In the Fe-BC (0.5:1), micro-scale particles existed mainly in the interior micropores of the flaky cracking BC surface (Fig. S1b). As the Fe loading increased, i.e., for Fe-BC (1:1), Fe particles with diameters ranging from micro- to nano-scale were present (Fig. S1c and e). These particles were evenly distributed in both micropores and on the surface of bulkier dendritic flocs, with an average particle size of 20–100 nm. Thus, BC can serve as a porous carbon support for Fe, increasing the dispersion of nanoparticles (NPs) (Han et al., 2015). In contrast, obvious particle aggregation into discrete spheres of ~10 μm was observed in the Fe-BC (2:1) (Fig. S1d), which is consistent with a previous finding that iron NPs tended to aggregate at an Fe/BC impregnation mass ratio of 4:1 (Yang et al., 2016; Zhu et al., 2017). EDX analysis revealed the co-existence of Fe, O, C, and Cl elements on the Fe-BC surfaces, suggesting the possible formation of iron (hydr)oxides.

The XRD patterns of the BC and Fe-BC composites are shown in Fig. 1a. In the case of the BC, the carbon matrix was highly graphitic, but the spectra of Fe-BC composites were less ordered because Fe likely decreased the graphitic order of the carbon structure, or masked the sharp carbon peaks due to surface Fe precipitation. As for Fe-BC composites, the characteristic peaks at 44.8° and 65.1° were assigned to α-Fe⁰ corresponding to the crystal planes of (110) and (200), respectively, indicating the formation of ZVI (Wu et al., 2015). However, the absence of an Fe oxide diffraction peak in the Fe-BC XRD pattern suggests the amorphous nature of iron (hydr)oxides and/or that their concentrations are below the detection limits of the XRD technique (Wu et al., 2015).

The Raman spectra of the BC and Fe-BC composites further elucidated physical characteristics of the carbonaceous materials, as shown in Fig. 1b. The two peaks at 1365 and 1585 cm⁻¹ correspond to the characteristic D and G bands of carbon, i.e., amorphous polyaromatic hydrocarbons and sp² C in graphitized carbon, respectively (Chia et al., 2012; Wang et al., 2017b). The intensity ratio of the D peak to the G peak (I_D/I_G) of the Fe-BC composites (0.93–1.01) is greater than that of the control BC (0.77), suggesting that the presence of Fe during the pyrolysis of BC induced more disordered defects within the BC structure

Table 2

Physical and chemical properties of BC and Fe-BC composites with different Fe/BC impregnation mass ratios (0.5:1, 1:1, and 2:1).

	BC	Fe-BC (0.5:1)	Fe-BC (1:1)	Fe-BC (2:1)
Fe (%) ^a	0.0877 ± 0.0001	26.2 ± 0.1	37.5 ± 1.1	54.2 ± 2.7
Ca (g kg ⁻¹) ^a	18.7 ± 0.5	12.6 ± 0.3	11.2 ± 0.2	8.10 ± 0.04
K (g kg ⁻¹) ^a	4.70 ± 0.20	1.50 ± 0.03	0.970 ± 0.020	0.730 ± 0.010
Mg (g kg ⁻¹) ^a	0.690 ± 0.040	0.360 ± 0.010	0.250 ± 0.010	0.100 ± 0.003
BET surface area, S _{BET} (m ² g ⁻¹)	227	223	172	138
Micropore surface area, S _{micro} (m ² g ⁻¹)	181	180	132	98.6
Internal surface area, S _{ext} (m ² g ⁻¹)	46.0	42.9	42.9	39.9
Total pore volume, V _{total} (cm ³ g ⁻¹)	0.133	0.133	0.123	0.104
Micropore volume, V _{micro} (cm ³ g ⁻¹)	0.0986	0.0977	0.0718	0.0538
V _{micro} /V _{total} (%)	74.2	73.2	58.5	51.6
Average pore diameter, D _p (nm)	2.34	2.39	2.80	3.01
pH ^b	9.70	5.60	5.20	5.20
CEC (meq kg ⁻¹) ^c	975	781	658	553
Zeta potential (mV) ^d	-36.1	14.1	21.2	26.0
pH _{pzc} ^e	4.90	5.40	5.50	5.60

^a Determined by total digestion (HNO₃ + HClO₄) and ICP-AES analysis.

^b 1 g solid + 20 mL DIW, 4-h end-over-end rotation (30 rpm), centrifugation (4000 rpm, 10 min), test supernatant pH.

^c Cation exchange capacity, determined by BaCl₂-MgSO₄ procedure.

^d 0.25 g solid + 25 mL DIW, 30-min sonication, determined by DLS Zetasizer.

^e pH value at point of zero charge in Day-90 FWW.

(Lawrinenko et al., 2017). This result is in good agreement with the XRD results.

3.2. Surface chemical behavior and thermal stability of Fe-BC composites

The FTIR spectra helped determine the functional groups on the surfaces of the BC and Fe-BC composites (Fig. 1c). In the case of the BC, the broad spectral band with a peak at 3440 cm⁻¹ was attributed to the presence of the -OH group (Cho et al., 2017b). A visible spectral band with a peak at 1116 cm⁻¹ was ascribed to C-O/C-O-C surface functional groups (Niazi et al., 2018). The small bands at 1583 and 1384 cm⁻¹ are consistent with aromatic rings (Oh et al., 2016), whereas methyl C-H bending occurring around 1434 cm⁻¹ and the peak at 875 cm⁻¹ are attributed to the C-H bands of aromatic species (Cho et al., 2017a; Mohan et al., 2015). After Fe impregnation, the bands decreased for C-O/C-O-C (1116 cm⁻¹) and C-H (1434 and 875 cm⁻¹), whereas an aromatic C=C band appeared at 1630 cm⁻¹ (Devi and Saroha, 2014). This result suggests that polymerization and carbonization of BC occurred during the synthesis of the Fe-BC

composites (Wang et al., 2017b), which accounted for more amorphous aromatic C observed in the Raman spectra. The bands at 680 and 470 cm⁻¹ were assigned to the Fe-O and C-Cl vibration modes (Devi and Saroha, 2015; Yan et al., 2013), respectively, indicating that Fe-O complexes and/or iron oxides existed/adhered on the surfaces of the Fe-BC composites, in addition to the presence of Fe⁰ revealed by XRD. The Fe-O might originate from Fe³⁺ hydrolysis after FeCl₃ pretreatment, which could chelate before pyrolysis and form a bidentate bridge with oxygen-containing functional groups of the BC (Wang et al., 2016; Yan et al., 2013). The increased intensity of the -OH band (3440 cm⁻¹) in the Fe-BC composites can be attributed to the presence of iron hydroxides on the BC surface (Qian et al., 2017; Tang et al., 2017).

The mass loss and thermal stability of the materials were evaluated by TGA (Fig. 1d1–2). The derivative thermogravimetry (DTG) peak shifted from 600 to 650 °C in the pattern of the BC to 750–950 °C in that of the Fe-BC composites (Fig. 1d2). This result is indicative of enhanced thermal stability upon the impregnation of Fe due to the formation of a C-O-Fe bond as inferred from the FTIR result (Li et al., 2014; Yang et al., 2016). There was a positive correlation between total mass loss at

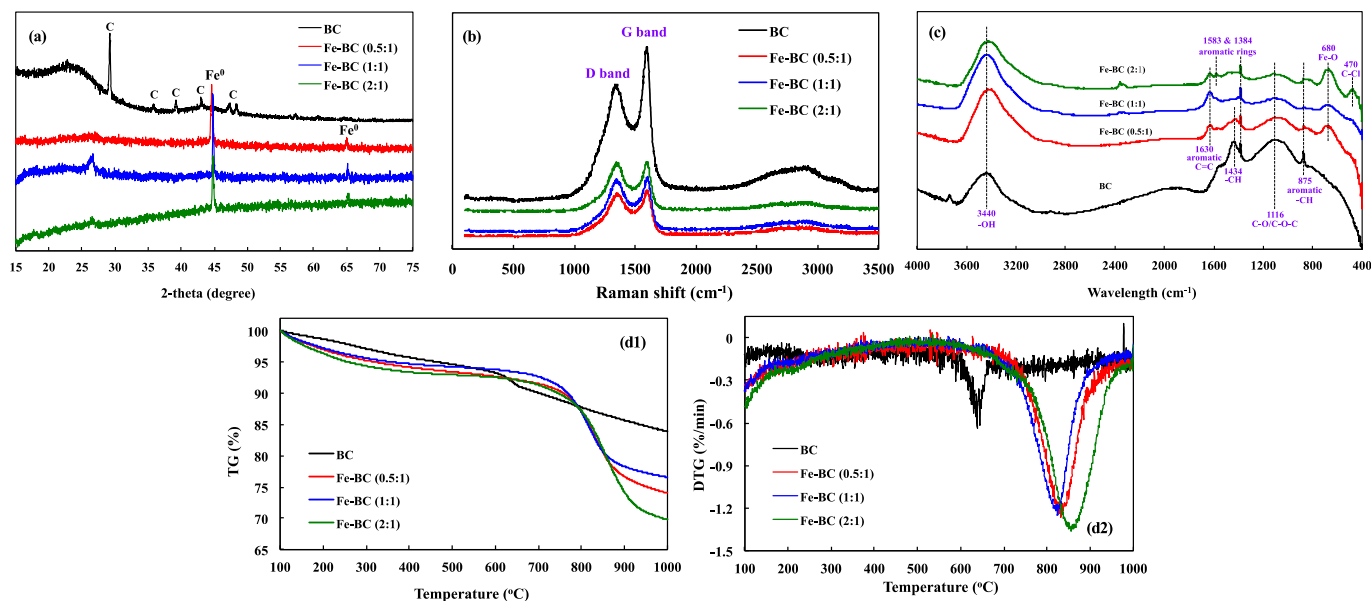


Fig. 1. XRD (a), Raman (b), FTIR (c), and TGA (d) analysis of BC and Fe-BC composites with different Fe/BC impregnation mass ratios (0.5:1, 1:1, and 2:1).

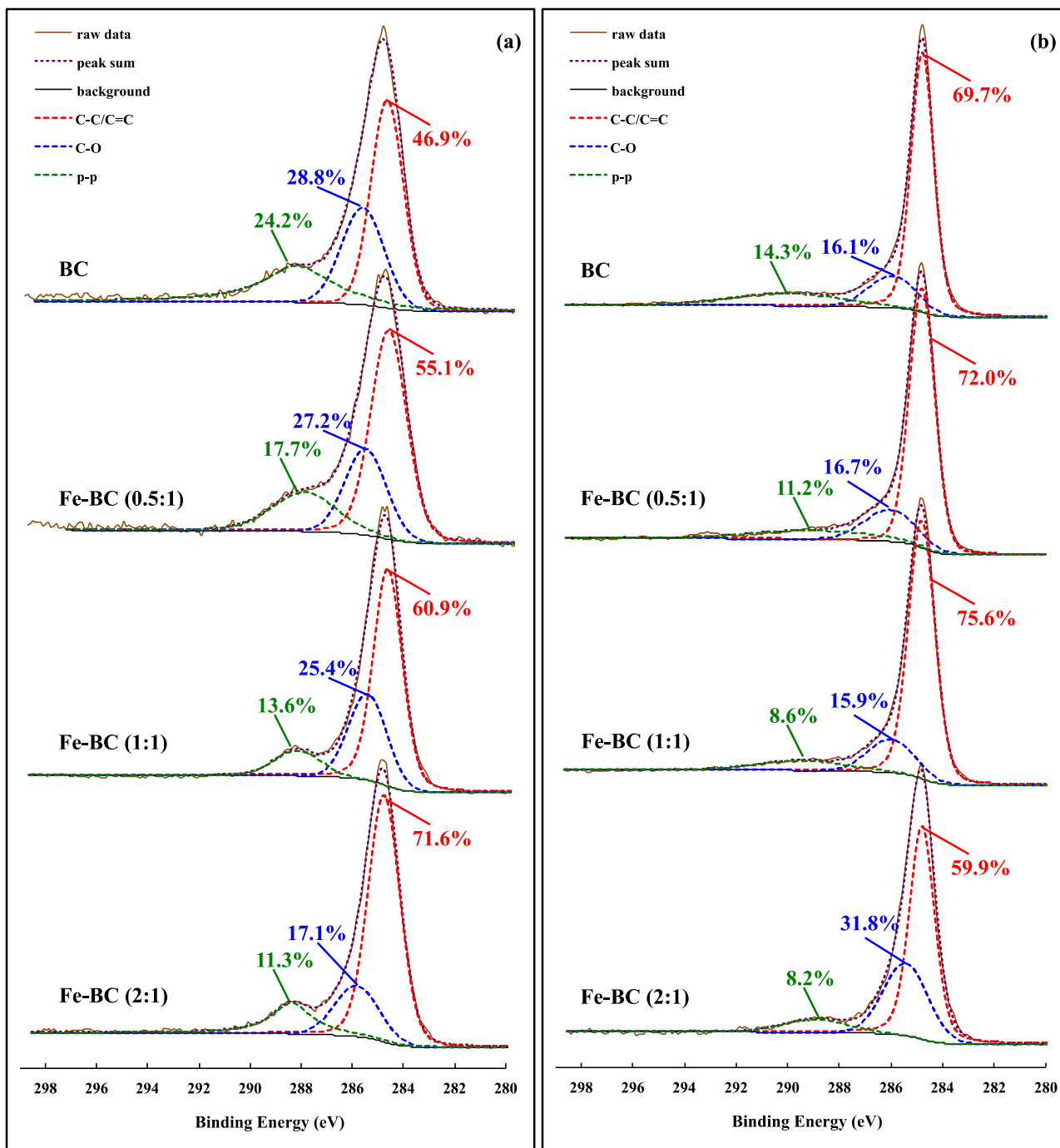


Fig. 2. XPS analysis of C 1s binding states of BC and Fe-BC composites with different Fe/BC impregnation mass ratios (0.5:1, 1:1, and 2:1) before (a) and after (b) Day-90 FWW treatment.

800–850 °C and Fe loading ratio (Fig. 1d1), which may correspond to the transformation of non-volatile Fe oxides and reduction to Fe⁰ in the Fe-BC composites (Wang et al., 2015).

The XPS survey showed that the BC was composed of C 1s and O 1s, whereas the Fe-BC composites incorporated C 1s, O 1s, and Fe 2p (Figs. 2a, S2a, and 3a). In all samples, the C 1s spectra were composed of three peaks that were assigned to C–C/C=C at 284.8 eV, C–O at 285.8 eV, and π - π^* transition in aromatic rings at 288.3 eV (Lau et al., 2017; Ling et al., 2017). As the Fe proportion increased, there was a decrease in the content of C–O (from 28.8 to 27.2–17.1%) and π - π^* (from 24.2 to 17.7–11.3%), whereas the content of C–C/C=C increased from 46.9% (BC) to 55.1–71.6% (Fe-BC composites) (Fig. 2a).

Therefore, C–O–Fe bonds formed as Fe impregnated BC by cation- π interaction and bidentate chelation with C–O (Wang et al., 2016), which was then broken by electron transfer during the pyrolysis to form C=C bonds or iron oxides, and ultimately the carbon structure was converted from a cross-linking to condensed or aromatic nature (Rawal et al., 2016).

In the Fe 2p spectra of the Fe-BC composites, the peaks at 724.2 and 727.2 eV were assigned to Fe²⁺ and Fe³⁺ (Fe 2p_{1/2}) in tetrahedral coordination, whereas 710.8 and 713.1 eV were assigned to Fe²⁺ and Fe³⁺ of Fe₃O₄ (Fe 2p_{3/2}) in octahedral coordination (Fig. 3a) (Tang et al., 2017). These results are consistent with the FTIR finding concerning the Fe–O species. In particular, the peak at 719.5 eV was

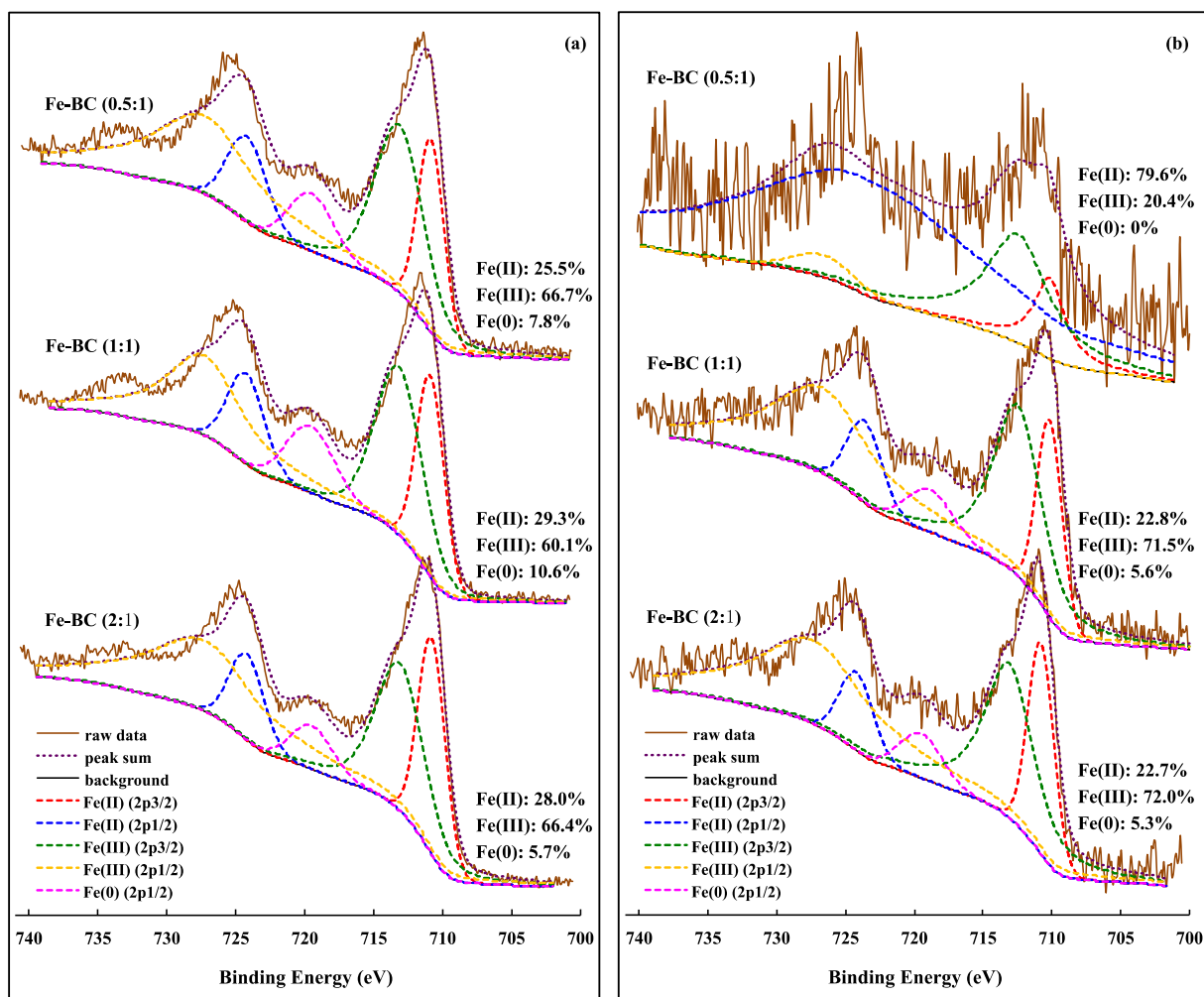
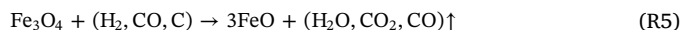
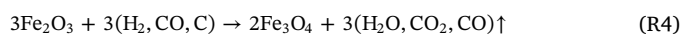
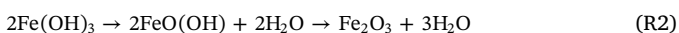
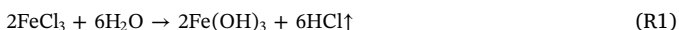


Fig. 3. XPS analysis of Fe 2p binding states of the Fe-BC composites with different Fe/BC impregnation mass ratios (0.5:1, 1:1, and 2:1) before (a) and after (b) Day-90 FWW treatment.

assigned to Fe⁰ (Fe 2p_{1/2}) (Tang et al., 2017), which upheld the successful reduction of Fe³⁺ to ZVI during pyrolysis, corroborating the evidence by XRD. Interestingly, the highest contents of Fe⁰ and Fe²⁺ (10.6% and 29.3%) were observed for the Fe-BC (1:1), followed by those of the Fe-BC (0.5:1) (7.8%, 25.5%) and Fe-BC (2:1) (5.7%, 28.0%). This observation corroborated the O 1s spectra depicting the lowest O–Fe ratio of 18.0% for the Fe-BC (1:1) (Fig. S2a). It can be inferred that the relatively low Fe loading would provide at best a thin shell to protect Fe⁰ from being exposed to O₂ during post-pyrolysis air stabilization (Zhu et al., 2017), whereas a higher Fe dosage led to notable Fe aggregation hindering its reduction to Fe⁰ during pyrolysis. An appropriate Fe impregnation relative to the BC support (e.g., the 1:1 mass ratio determined in this study) is critical for the homogeneity of Fe⁰ NPs formation in the Fe-BC composites (Fig. S1).

The whole oxide reduction mechanism via carbon and gaseous intermediates for the Fe-BC synthesis can be summarized as follows. First, iron salts are converted into iron oxide (R1, R2) (Zhang et al., 2017), which is then carbothermally reduced into magnetite at 400–500 °C (R3, R4) (Wang et al., 2015). This is then directly converted into iron protioxide (R3, R5) and iron carbide (R6) at 650 and 800 °C, respectively. Furthermore, decomposition of iron carbide to elemental iron sets in between 900 and 1000 °C (R7) (Shen, 2015).



3.3. Fe-BC performance for removal of potentially toxic elements

The simultaneous time-dependent removals of Cu(II), Cr(VI), Zn(II), and As(V) in Day-90 FWW by the Fe-BC composites were investigated (Fig. 4a). The removal kinetics exhibited a transition from a fast initial rate during 0–1 h to a slower rate for 1–2 h, and then an apparent maximum at 4–8 h. The maximum removal efficiencies were generally greater for the Fe-BC composites as compared with the control BC (Fig. 4b). In particular, Cu(II) removal was significantly promoted ($p < 0.05$) from $68.3 \pm 0.1\%$ to $97.8 \pm 0.2\%$ – $99.1 \pm 0.1\%$ in the presence of Fe-BC. A pronounced Cr(VI) removal (88.2%) ($p < 0.05$) was observed at the highest Fe loading, i.e., Fe-BC (2:1) (vs. $56.4 \pm 0.9\%$ – $58.4 \pm 0.5\%$ for the rest of the materials). The stable complex of $\text{CaCrO}_4(\text{aq})$ as the suggested major Cr(VI) species in Day-90 FWW (Table S1) may require a high Fe loading for significant removal. The As(V) removal by the Fe-BC composites ($65.9 \pm 0.5\%$ – $77.7 \pm 0.1\%$) was greater ($p < 0.05$) than that of the

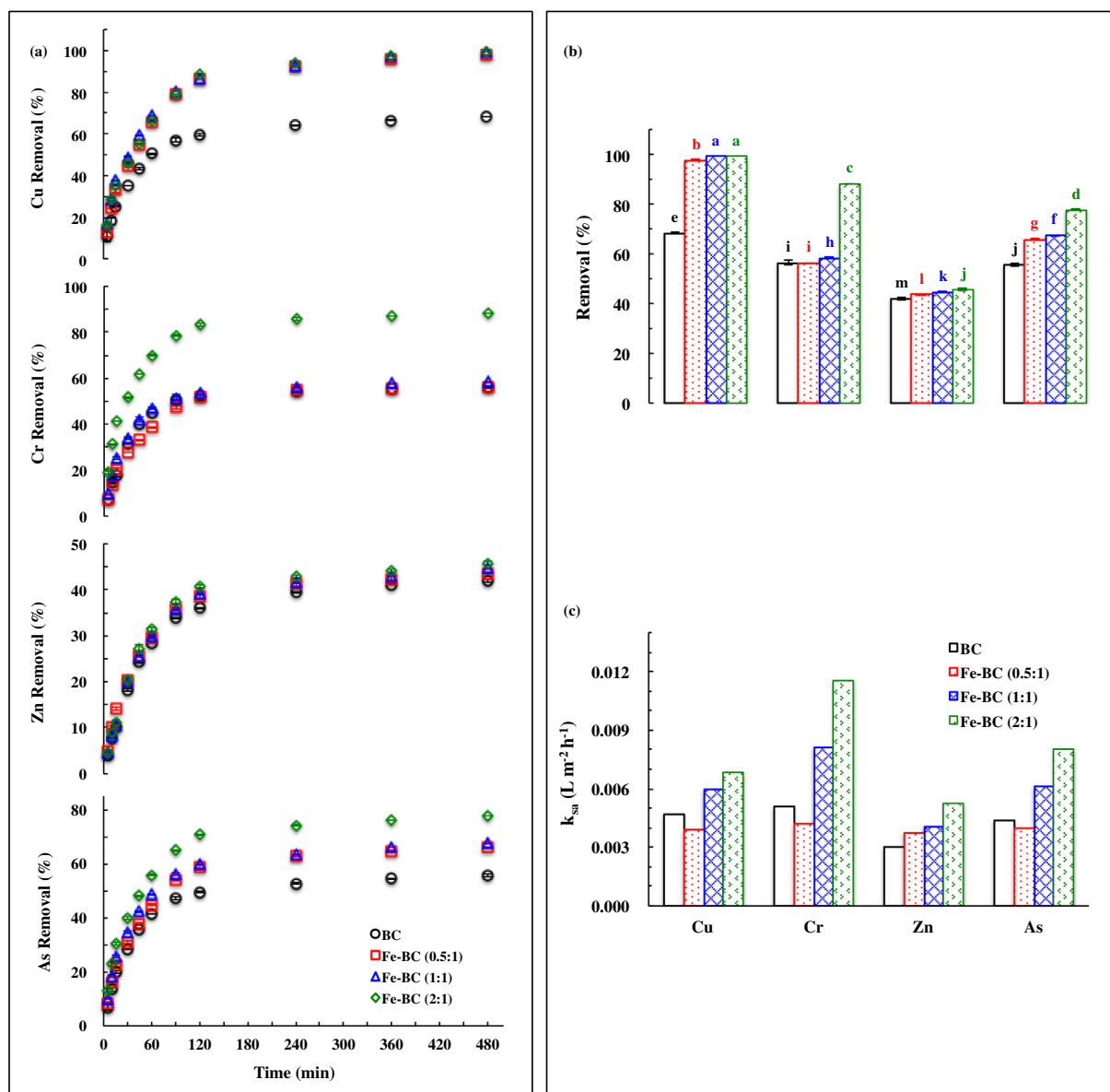


Fig. 4. Time-dependent (a), 8-h (b), and pseudo-second-order rate constants (k_{sa}) (c) of potential toxic elements (Cu, Cr, Zn, and As) removal from Day-90 FWW by BC and Fe-BC composites with different Fe/BC impregnation mass ratios (0.5:1, 1:1, and 2:1) (lower-case letters indicate the significance levels ($p < 0.05$) of differences in the results).

BC ($55.6 \pm 0.2\%$) and increased with the Fe content. In contrast, Fe-BCs marginally enhanced the Zn(II) removal (from $42.0 \pm 0.5\%$ to $43.6 \pm 0.2\%$ – $45.8 \pm 0.6\%$). The kinetics data were fitted using a pseudo-second-order kinetics model (Supporting information) and the surface area-normalized rate constant (k_{sa}) (Fig. 4c and Table S3) suggested the accelerated removal after Fe impregnation, except for Fe-BC (0.5:1) in the cases of Cu(II), Cr(VI), and As(V) removal.

The XPS analyses of the spent materials showed a characteristic peak at 934.5 eV for the control BC, which could be attributed to the surface adsorption of Cu^{2+} (Fig. S3a). The two new peaks at 932.4 and 935.5 eV for the Fe-BC composites represented Cu^0 and $\equiv FeCuO_2^+$, respectively (Qiu et al., 2012), suggesting that Fe^0 facilitated Cu(II) removal through reduction (*viz.* $Fe^0 \rightarrow Fe^{2+}/Fe^{3+} + (2-3) e^-$; $Cu^{2+} + 2 e^- \rightarrow Cu^0$) and complexation with the detached/attached colloidal Fe^{3+} (*viz.* $Cu^{2+} + Fe^{3+} + 4OH^- \rightarrow FeCuO_2^+ + 2H_2O$). The peak areas for Cu^0 (6.8%, 14.8%, and 25.7%) and $\equiv FeCuO_2^+$ (18.2%, 34.2%, and 67.1%) substantially increased, whereas those for Cu^{2+} (75.0%, 51.0%, and 7.2%) gradually decreased with an increase in Fe

content of 1:0.5, 1:1, and 1:2, respectively. Surface adsorption was the primary mechanism for Cu(II) removal by the BC ($227.3 m^2 g^{-1}$) and Fe-BC (0.5:1) ($223.0 m^2 g^{-1}$), where the negatively charged surface (solution pH $> pH_{pzc}$, Table 2 and Fig. S5) favored the adsorption of $CuCl^+$ and Cu^{2+} (73.4% in total; Table S1). The contribution of Fe^0 to Cu(II) removal was enhanced by increasing Fe loading. In combination with the increasing removal rate with Fe loading (Fig. 4c), these observations imply that the Cu(II) removal *via* reduction and complexation could be faster than adsorption, whereas the removal capacity approached 100% regardless of the dominant mechanisms (Fig. 4b).

In the Cr 2p spectra, while only one peak representing Cr(VI) at 580.79 eV was observed for the control BC (Biesinger et al., 2011), three new peaks at 577.3, 577.9, and 579.4 eV were deconvoluted on the Fe-BC composites that can be assigned to $Cr(OH)_3$ (Biesinger et al., 2011), $FeCr_2O_4$ (Chowdhury et al., 2012), and CrO_4^{2-} (Abdel-Samad and Watson, 1997), respectively (Fig. S3b). The contribution of Cr(III) was increased in the form of $Cr(OH)_3$ (40.5 and 48.3%) and $FeCr_2O_4$ (28.4 and 24.9%) as Fe increased from 0.5:1 to 1:1. With a higher Fe

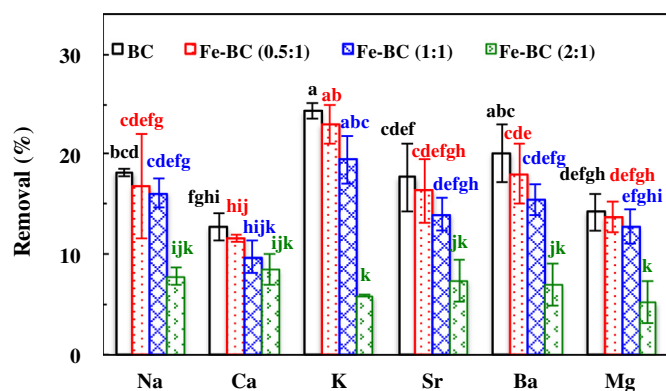


Fig. 5. The 8-h removal of cations (Na, Ca, K, Mg, Sr, and Ba) from Day-90 FWW by BC and Fe-BC composites with different Fe/BC impregnation mass ratios (0.5:1, 1:1, and 2:1) (lower-case letters indicate the significance levels ($p < 0.05$) of differences in the results).

loading at 2:1, the $\text{Cr}(\text{OH})_3$ peak disappeared leaving FeCr_2O_4 (78.7%) as the dominating species. These findings suggest that $\text{Cr}(\text{VI})$ was removed via reduction by Fe^0 on Fe-BC composites (viz. $\text{Cr}(\text{VI}) + 3\text{e}^- \rightarrow \text{Cr}^{3+}$), followed by (co-)precipitation with detached/attached colloidal Fe^{2+} (viz. $\text{Cr}^{3+} + 3\text{OH}^- \rightarrow \text{Cr}(\text{OH})_3$; $2\text{Cr}^{3+} + \text{Fe}^{2+} + 8\text{OH}^- \rightarrow \text{FeCr}_2\text{O}_4 + 4\text{H}_2\text{O}$), and adsorption onto the Fe-BC and/or the iron (hydr)oxide surface (Rajapaksha et al., 2018). While $\text{Cr}(\text{VI})$ reduction by Fe^0 was the predominant removal mechanism in general, coordination with detached/attached colloidal Fe^{2+} became important at the highest Fe loading ratio (2:1), resulting in significantly enhanced ($p < 0.05$) removal capacity (Fig. 4b).

In contrast, surface adsorption remained the major pathway for Zn (II) removal by BC, Fe-BC (0.5:1), and Fe-BC (1:1), due to the high contribution of Zn^{2+} (1022.4 eV; Gan et al., 2015), i.e., 100%, 57%, and 55.5%, respectively (Fig. S4a). The dominating anionic Zn(II) species in Day-90 FWW (ZnCl_3^- and ZnCl_4^{2-} of 80% in total, Table S1) may incur electrostatic repulsion against the negatively charged BC or Fe-BC surfaces, hindering Zn(II) removal by adsorption (Fig. 4b). Nevertheless, removal via Zn(II) complexation with detached/attached colloidal Fe^{3+} (viz. $\text{Zn}^{2+} + 2\text{Fe}^{3+} + 8\text{OH}^- \rightarrow \text{ZnFe}_2\text{O}_4 + 4\text{H}_2\text{O}$) became more significant with higher Fe content, in view of the increased proportion (43.0–60.2%) of ZnFe_2O_4 at 1021.4 eV (Bera et al., 2001), which explained the improved removal kinetics (Fig. 4c).

Inner-sphere ligand exchange was demonstrated as the common mechanism for As(V) adsorption by the BC and Fe-BC (0.5:1 and 1:1). As depicted in Fig. S4b, for BC, As(V) in the form of H_2AsO_4^- at 45.7 eV gradually developed into HAsO_4^{2-} (44.8 eV, 29.6%) and AsO_4^{3-} (44.0 eV, 34.9%) (Bang et al., 2005). A higher Fe impregnation ratio (1:1) promoted the formation of AsO_4^{3-} (44.4–52.6%) with a lower proportion of HAsO_4^{2-} (23.5–24.7%). Fe impregnation might induce more defects within the BC structure as evidenced by XRD and Raman analyses, which can promote electron transfer (viz. $\text{H}_2\text{AsO}_4^- + \text{e}^- \rightarrow \text{HAsO}_4^{2-} + \text{e}^- \rightarrow \text{AsO}_4^{3-}$) in the adsorption process (Lawrinenko et al., 2017; Yan et al., 2015). In addition, H_2AsO_4^- completely developed into AsO_4^{3-} (80.7%) on the Fe-BC (2:1), suggesting the formation of various Fe–O–As(V) complexes as the primary mechanism for the adsorption of As(V) (Bakshi et al., 2018; Zhang et al., 2017), because Fe–O species on the Fe-BC composites were observed by FTIR and XPS. Such complexation was associated with the positive correlation between the As(V) removal capacity and the Fe content (Fig. 4b) and the enhanced removal kinetics (Fig. 4c).

The Fe 2p binding states on the Fe-BC composites before and after Day-90 FWW treatment are compared in Fig. 3. The lowest Fe content on the BC surface, 7.8% Fe^0 on Fe-BC (0.5:1) (Fig. 3a), was completely exhausted in serving as electron donor, resulting in a large amount of Fe^{2+} (79.6%). As shown in Fig. S1b, a thin layer of Fe particles was

embedded on tubular channels of the BC surface; thus, the Fe-mediated reaction was probably rate-limited by intraparticle diffusion, accounting for the slowest kinetics for Cu(II), Cr(VI), and As(V). In comparison, for the Fe-BC (1:1), both Fe^0 (10.6%) and Fe^{2+} (29.3%) (Fig. 3a) provided electrons for the reduction/charge-transfer process, with 5.6% and 22.8% remained after the reaction (Fig. 3b). The homogeneous distribution of Fe^0 on the BC surface with the Fe/BC mass ratio of 1:1 accounted for the highest $\text{Fe}^0/\text{Fe}^{2+}$ ratio for the optimal reduction/charge-transfer efficiency. Nevertheless, Fe^{2+} (28.0–22.7%) played a vital part in the electron transfer, with negligible Fe^0 loss (5.7–5.3%) observed during the FWW treatment by the Fe-BC (2:1). This resulted in the lowest reduction/charge-transfer reactivity of the Fe-BC (2:1). Hence, (co-)precipitation and complexation were the major removal pathways owing to severe aggregation of Fe^0 on the BC surface at this highest Fe loading. The analysis of O 1s binding states on the Fe-BC (2:1) demonstrated an obvious decrease in Fe–O from 47.4 to 25.6% after reaction (Fig. S2b), indicating possible detachment of (co-)precipitated Fe from the Fe-BC surface, in contrast to the increase of 27.5–29.2% and 18.0–27.1% on the Fe-BC (0.5:1) and Fe-BC (1:1), respectively. The major removal mechanisms of potentially toxic elements by the Fe-BC composites are illustrated in Scheme 1 (Supporting information).

3.4. Fe-BC performance for removal of inherent cations

The removal efficiencies of inherent cations (Na, Ca, K, Mg, Sr, and Ba) from Day-90 FWW by the Fe-BC composites after the 8-h reaction are shown in Fig. 5. The Fe impregnation reduced ($p < 0.05$) the removal of Na (from $18.2 \pm 0.4\%$ to $16.7 \pm 5.2\%$ – $7.8 \pm 0.9\%$), Ca (from $12.7 \pm 1.4\%$ to $11.7 \pm 0.4\%$ – $8.5 \pm 1.6\%$), K (from $24.3 \pm 0.8\%$ to $23.0 \pm 1.9\%$ – $5.9 \pm 0.1\%$), Mg (from $14.2 \pm 1.9\%$ to $13.7 \pm 1.5\%$ – $5.2 \pm 2.1\%$), Sr (from $17.7 \pm 3.4\%$ to $16.4 \pm 3.2\%$ – $7.4 \pm 2.1\%$), and Ba (from $20.1 \pm 2.9\%$ to $18.0 \pm 3.0\%$ – $7.0 \pm 2.1\%$). Nevertheless, the removal capacity in this study was equivalent to 3.2–7.2 g cations per gram of the Fe-BC composites. These values are superior to the NaOH-modified zeolite (0.14 g Ca and Mg removal per gram of zeolite) (Chang et al., 2017) and pinewood-derived biochar (0.5 g TDS removal per gram of biochar) (Lobo et al., 2016) found in previous studies of FWW treatment. The cations could have been removed by the Fe-BC composites via surface adsorption through electrostatic interaction (Zhu et al., 2017), chelation with oxygen containing groups (Bogusz et al., 2015), cation- π interaction (Pi et al., 2015), and colloidal coagulation.

The increasing positive charge with Fe loading over the Fe-BC surface (Table 2) may have resulted in electrostatic repulsive force impeding cation adsorption. In addition, the development of iron (hydr) oxides ($\text{Fe}_3\text{O}_4/\gamma\text{-Fe}_2\text{O}_3$, $\gamma\text{-FeOOH}$, and $\alpha\text{-FeOOH}/\alpha\text{-Fe}_2\text{O}_3$) after Day-90 FWW treatment (Bakshi et al., 2018), as evidenced by Raman analysis (Fig. 6a), may block the active/sorption sites on the Fe-BC surface. The C 1s spectrum of control BC (Fig. 2b) revealed an obvious decrease in C–O (from 28.8 to 16.1%) and $\pi\text{-}\pi^*$ (from 24.2 to 14.3%) interactions after reaction, which could be attributed to divalent and monovalent cation removal (Mohan et al., 2015). Similar trends were also observed on the Fe-BC (0.5:1) and Fe-BC (1:1) (Fig. 2b). The FTIR spectra (Fig. 6b) indicated the disappearance of broad peaks near $1109\text{--}1117\text{ cm}^{-1}$ (C–O/C–O–C) with emerging small peaks within $984\text{--}1206\text{ cm}^{-1}$ (C–O–Metal) (Niazi et al., 2018). The intensity ratios of the G peak to the D peak (I_G/I_D) decreased in the Raman spectra of the BC (from 1.30 to 1.29) and the Fe-BC composites (from 1.08–0.99 to 1.04–0.84) after the reaction (Fig. 6a), reaffirming the usage of sp^2 C in $\pi\text{-}\pi$ transitions for inherent cation removal. However, the consumption of C–C/C=C (from 71.6% to 59.9%) was more pronounced than that in $\pi\text{-}\pi^*$ (from 11.3% to 8.2%) on Fe-BC (2:1) (Fig. 2b). The speciation modeling results in Table S2 suggested that divalent cations were primarily coordinated with Cl^- as CaCl^+ , MgCl^+ , SrCl^+ , and BaCl^+ in Day-90 FWW, and that the positively charged surface sites (C–C $^+$ /

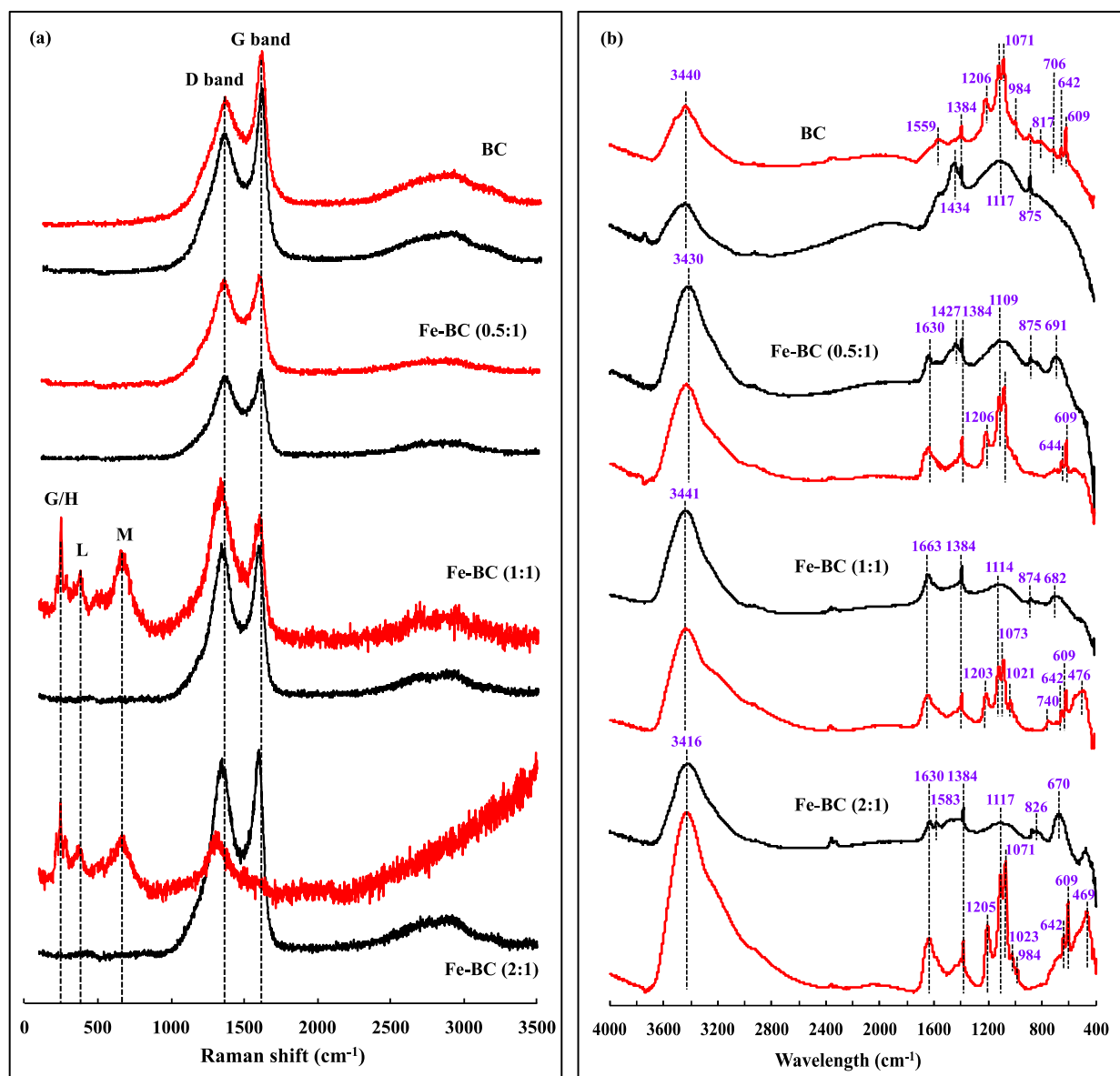


Fig. 6. (a) Raman and (b) FTIR analysis of BC and Fe-BC composites with different Fe/BC impregnation mass ratios (0.5:1, 1:1, and 2:1) before (—) and after (—) Day-90 FWW treatment. Major peaks correspond to magnetite/maghemite ($\text{Fe}_3\text{O}_4/\gamma\text{-Fe}_2\text{O}_3$) (M), lepidocrocite ($\gamma\text{-FeOOH}$) (L), and goethite/hematite ($\alpha\text{-FeOOH}/\alpha\text{-Fe}_2\text{O}_3$) (G/H).

$\text{C}=\text{C}^+$) were occupied by Cl^- , corroborating the new peaks at $469\text{--}642\text{ cm}^{-1}$ of FTIR spectra (Devi and Saroha, 2015) after the reaction (Fig. 6b). This was consistent with the lowest removal of the divalent cations (Ca^{2+} , Mg^{2+} , Sr^{2+} , and Ba^{2+}) by the Fe-BC (2:1) in Fig. 5. The main removal mechanisms of the inherent cations by the Fe-BC composites are also shown in Scheme 1 (Supporting information).

3.5. Fe-BC performance for 1,1,2-TCA and TOC removal

In addition to the inorganic contaminants discussed above, the co-existing organic pollutants should also be addressed for comprehensive FWW treatment. The time-dependent removal of 1,1,2-TCA by the Fe-BC composites (Fig. 7a) exhibited a transition from a fast initial rate during 0–1 h, to a slower rate for 1–2 h, and then to an apparent maximum at 4–8 h. The maximum removal efficiency (Fig. 7b) was obviously enhanced for the Fe-BC composites ($76.6 \pm 1.6\%$ – $91.0 \pm 0.8\%$) ($p < 0.05$) and increased with Fe content, when compared with the control BC ($62.2 \pm 2.4\%$). Notably,

1,1,2-TCA was primarily removed by the BC through adsorption ($59.2 \pm 3.7\%$, which was further promoted on the Fe-BC composites ($66.4 \pm 2.8\%$ – $68.3 \pm 2.8\%$) ($p < 0.05$). The maximum coverage of loaded Fe (estimated by $\text{mol}_{\text{Fe}} \times N_{\text{A}} \times \pi r_{\text{ionic-Fe}}^2 / S_{\text{A-biochar}}$) reached 16.5%, 27.3%, and 52.4% on the Fe-BC (0.5:1, 1:1, and 2:1), respectively. The Fe^0 -mediated 1,1,2-TCA reduction via dechlorination was significantly promoted from $9.3 \pm 0.1\%$ to $24.6 \pm 2.1\%$ ($p < 0.05$) by a higher Fe content (Fig. 7a and b). The large specific surface area of BC may facilitate the mass transfer of contaminants from the ambient solution to the surface of Fe-BC for adsorption and reduction (Pi et al., 2015). Nevertheless, intraparticle diffusion was probably the rate-limiting step for 1,1,2-TCA removal by the Fe-BC (0.5:1) (Fig. 7c), and the reduction process was limited by the development of surface precipitated iron (hydr)oxides on the Fe-BC (2:1) that would hinder the electron transfer to 1,1,2-TCA after its adsorption (Lawrinenko et al., 2017; Li et al., 2017).

Compared with the maximum TOC removal of Day-90 FWW by the BC ($3.9 \pm 1.0\%$), the removal was unexpectedly enhanced

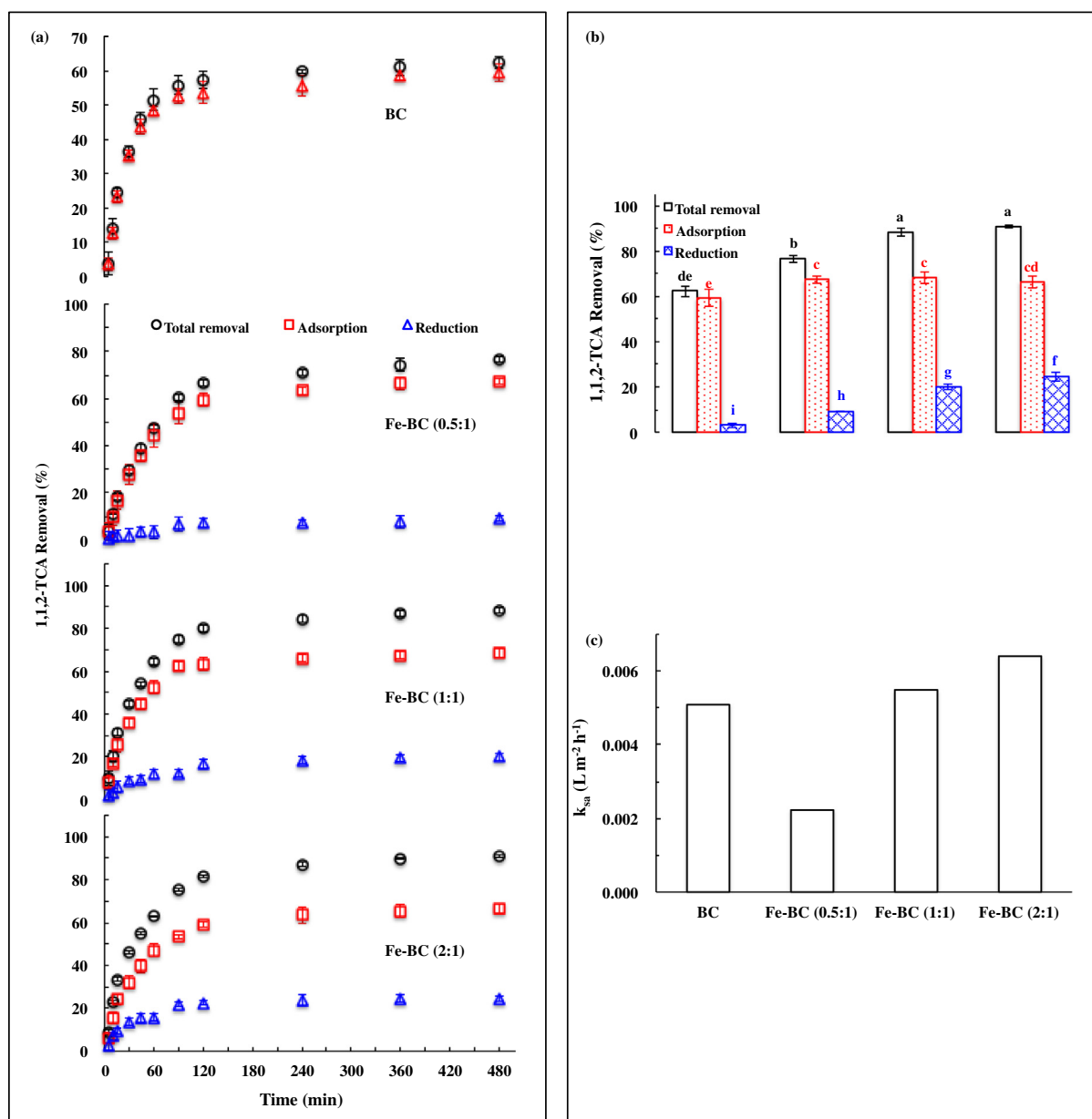


Fig. 7. Time-dependent (a), 8-h (b), and pseudo-second-order rate constants (k_{sa}) (c) of 1,1,2-TCA removal from Day-90 FWW by BC and Fe-BC composites with different Fe/BC impregnation mass ratios (1:0.5, 1:1, and 1:2) (lower-case letters indicate the significance levels ($p < 0.05$) of differences in the results).

($5.4 \pm 0.8\%$ – $11.2 \pm 1.3\%$) by the Fe-BC composites with increasing Fe content (Fig. S6). In light of the continuous Fe loss (possibly in forms of colloidal Fe, 222.9 ± 7.2 – $289.6 \pm 1.3 \text{ mg L}^{-1}$) from the Fe-BC composites during the 8-h reaction (Fig. S7), the organic compounds in Day-90 FWW (e.g., polyacrylamide, Table 1) may have been removed through coagulation/flocculation *via* crosslinking with detached colloidal Fe as the major mechanism (Lee et al., 2015). Moreover, the more positively charged surface of the Fe-BC composites with increasing Fe content (Table 2) may also facilitate the removal of anionic organics. Such detached Fe fraction in practice would need to be collected by sedimentation to alleviate potential Fe toxicity (Lei et al., 2018b). The main removal mechanisms of 1,1,2-TCA and organic compounds (as indicated by TOC) by the Fe-BC composites are shown in Scheme 1 (Supporting information).

4. Conclusions

Through the integrated analysis of the surface characteristics and

contaminant interactions, we demonstrated that the Fe-BC composites (especially for 1:1 mass ratio) exhibited a superior performance for the simultaneous removal of potentially toxic elements, inherent cations, 1,1,2-TCA, and organic compounds from high-salinity FWW. The sustainability features of the Fe-BC composites are highlighted as follows: (i) Fe-BC composites improved the thermal stability compared with pristine BC; (ii) Fe-BC composites with an appropriate Fe/BC impregnation mass ratio (1:1) mitigated oxidation and aggregation of Fe^0 ; (iii) Fe-BC composites were capable of simultaneous removal of multiple contaminants from the FWW owing to the complementary adsorptive, reductive, and complexing characteristics of the BC and Fe. Therefore, the Fe-BC composites are fast, sustainable, and potentially low-cost sorbent applicable for effective (pre-)treatment of FWW.

Acknowledgement

The authors appreciate the financial support from the Hong Kong Research Grants Council (PolyU 15217818 and E-PolyU503/17) for this

study.

Appendix A. Supplementary data

Supplementary data to this article can be found online at <https://doi.org/10.1016/j.envint.2019.01.047>.

References

- Abass, O.K., Zhuo, M., Zhang, K., 2017. Concomitant degradation of complex organics and metals recovery from fracking wastewater: roles of nano zerovalent iron initiated oxidation and adsorption. *Chem. Eng. J.* 328, 159–171.
- Abdel-Samad, H., Watson, P.R., 1997. An XPS study of the adsorption of chromate on goethite (α -FeOOH). *Appl. Surf. Sci.* 108, 371–377.
- Abualfaraj, N., Gurian, P.L., Olson, M.S., 2014. Characterization of Marcellus shale flowback water. *Environ. Eng. Sci.* 31, 514–524.
- Bakshi, S., Banik, C., Rathke, S.J., Laird, D.A., 2018. Arsenic sorption on zero-valent iron-biochar complexes. *Water Res.* 137, 153–163.
- Bang, S., Johnson, M.D., Korfiatis, G.P., Meng, X., 2005. Chemical reactions between arsenic and zero-valent iron in water. *Water Res.* 39, 763–770.
- Bera, S., Prince, A.A.M., Velmurugan, S., Raghavan, P.S., Gopalan, R., Pannierselvan, G., Narasimhan, S.V., 2001. Formation of zinc ferrite by solid-state reaction and its characterization by XRD and XPS. *J. Mater. Sci.* 36, 5379–5384.
- Biesinger, M.C., Payne, B.P., Grosvenor, A.P., Lau, L.W., Gerson, A.R., Smart, R.S.C., 2011. Resolving surface chemical states in XPS analysis of first row transition metals, oxides and hydroxides: Cr, Mn, Fe, Co and Ni. *Appl. Surf. Sci.* 257, 2717–2730.
- Blewett, T.A., Delompre, P.L.M., He, Y., Folkerts, E.J., Flynn, S.L., Alessi, D.S., Goss, G.G., 2017. The sub-lethal and reproductive effects of acute and chronic exposure to flowback and produced water from hydraulic fracturing on the water flea *Daphnia magna*. *Environ. Sci. Technol.* 51, 3032–3039.
- Bogusz, A., Oleszczuk, P., Dobrowolski, R., 2015. Application of laboratory prepared and commercially available biochars to adsorption of cadmium, copper and zinc ions from water. *Bioresour. Technol.* 196, 540–549.
- Butkovskiy, A., Bruning, H., Kools, S.A., Rijnaarts, H.H., van Wezel, A.P., 2017. Organic pollutants in shale gas flowback and produced waters: identification, potential ecological impact and implications for treatment strategies. *Environ. Sci. Technol.* 51, 4740–4754.
- Butkovskiy, A., Faber, A.H., Wang, Y., Grolle, K., Hofman-Caris, R., Bruning, H., Van Wezel, A.P., Rijnaarts, H.H., 2018. Removal of organic compounds from shale gas flowback water. *Water Res.* 138, 47–55.
- Camarillo, M.K., Domen, J.K., Stringfellow, W.T., 2016. Physical-chemical evaluation of hydraulic fracturing chemicals in the context of produced water treatment. *J. Environ. Manag.* 183, 164–174.
- Chang, H., Liu, T., He, Q., Li, D., Crittenden, J., Liu, B., 2017. Removal of calcium and magnesium ions from shale gas flowback water by chemically activated zeolite. *Water Sci. Technol.* 76, 575–583.
- Chen, S.S., Sun, Y.Q., Tsang, D.C.W., Graham, N.J.D., Ok, Y.S., Feng, Y.J., Li, X.D., 2016. Potential impact of flowback water from hydraulic fracturing on agricultural soil quality: metal/metalloid bioaccessibility, Microtox bioassay, and enzyme activities. *Sci. Total Environ.* 579, 1419–1426.
- Chen, S.S., Sun, Y.Q., Tsang, D.C.W., Graham, N.J.D., Ok, Y.S., Feng, Y.J., Li, X.D., 2017. Insights into the subsurface transport of As(V) and Se(VI) in produced water from hydraulic fracturing using soil samples from Qingshankou Formation, Songliao Basin, China. *Environ. Pollut.* 223, 449–456.
- Chia, C.H., Gong, B., Joseph, S.D., Marjo, C.E., Munroe, P., Rich, A.M., 2012. Imaging of mineral-enriched biochar by FTIR, Raman and SEM-EDX. *Vib. Spectrosc.* 62, 248–257.
- Cho, D.W., Kwon, G., Yoon, K., Tsang, Y.F., Ok, Y.S., Kwon, E.E., Song, H., 2017a. Simultaneous production of syngas and magnetic biochar via pyrolysis of paper mill sludge using CO₂ as reaction medium. *Energy Convers. Manag.* 145, 1–9.
- Cho, D.W., Yoon, K., Kwon, E.E., Biswas, J.K., Song, H., 2017b. Fabrication of magnetic biochar as a treatment medium for As(V) via pyrolysis of FeCl₃-pretreated spent coffee ground. *Environ. Pollut.* 229, 942–949.
- Chowdhury, S.R., Yanful, E.K., Pratt, A.R., 2012. Chemical states in XPS and Raman analysis during removal of Cr (VI) from contaminated water by mixed maghemite–magnetite nanoparticles. *J. Hazard. Mater.* 235, 246–256.
- Devi, P., Saroha, A.K., 2014. Synthesis of the magnetic biochar composites for use as an adsorbent for the removal of pentachlorophenol from the effluent. *Bioresour. Technol.* 169, 525–531.
- Devi, P., Saroha, A.K., 2015. Simultaneous adsorption and dechlorination of pentachlorophenol from effluent by Ni-ZVI magnetic biochar composites synthesized from paper mill sludge. *Chem. Eng. J.* 271, 195–203.
- Dong, H., Deng, J., Xie, Y., Zhang, C., Jiang, Z., Cheng, Y., Hou, K.J., Zeng, G., 2017. Stabilization of nanoscale zero-valent iron (nZVI) with modified biochar for Cr (VI) removal from aqueous solution. *J. Hazard. Mater.* 332, 79–86.
- Gan, C., Liu, Y., Tan, X., Wang, S., Zeng, G., Zheng, B., Li, T.T., Jiang, Z.J., Liu, W., 2015. Effect of porous zinc-biochar nanocomposites on Cr (VI) adsorption from aqueous solution. *RSC Adv.* 5, 35107–35115.
- Han, L., Xue, S., Zhao, S., Yan, J., Qian, L., Chen, M., 2015. Biochar supported nanoscale iron particles for the efficient removal of methyl orange dye in aqueous solutions. *PLoS One* 10, e0132067.
- Hayes, T., 2009. Sampling and Analysis of Water Streams Associated With the Development of Marcellus Shale Gas. Final report Prepared for the Marcellus Shale Coalition. (December 2009).
- Kausley, S.B., Malhotra, C.P., Pandit, A.B., 2017. Treatment and reuse of shale gas wastewater: electrocoagulation system for enhanced removal of organic contamination and cation causing divalent cations. *J. Water Process Eng.* 16, 149–162.
- Lau, A.Y., Tsang, D.C.W., Graham, N.J.D., Ok, Y.S., Yang, X., Li, X.D., 2017. Surface-modified biochar in a bioretention system for *Escherichia coli* removal from stormwater. *Chemosphere* 169, 89–98.
- Lawrinenko, M., Laird, D.A., Van Leeuwen, J.H., 2016. Sustainable pyrolytic production of zerovalent iron. *ACS Sustain. Chem. Eng.* 5, 767–773.
- Lawrinenko, M., Wang, Z., Horton, R., Mendivelso-Perez, D., Smith, E.A., Webster, T.E., Larid, D.A., Van Leeuwen, J.H., 2017. Macroporous carbon supported zerovalent iron for remediation of trichloroethylene. *ACS Sustain. Chem. Eng.* 5, 1586–1593.
- Lee, S.S., Shah, H.S., Awad, Y.M., Kumar, S., Ok, Y.S., 2015. Synergy effects of biochar and polyacrylamide on plants growth and soil erosion control. *Environ. Earth Sci.* 74, 2463–2473.
- Lei, C., Sun, Y.Q., Khan, E., Chen, S.S., Tsang, D.C.W., Graham, N.J.D., Ok, Y.S., Yang, X., Lin, D.H., Feng, Y.J., Li, X.D., 2018a. Removal of chlorinated organic solvents from hydraulic fracturing wastewater by bare and entrapped nanoscale zero-valent iron. *Chemosphere* 196, 9–17.
- Lei, C., Sun, Y.Q., Tsang, D.C.W., Lin, D.H., 2018b. Environmental transformations and ecological effects of iron-based nanoparticles. *Environ. Pollut.* 232, 10–30.
- Li, F., Cao, X., Zhao, L., Wang, J., Ding, Z., 2014. Effects of mineral additives on biochar formation: carbon retention, stability, and properties. *Environ. Sci. Technol.* 48, 11211–11217.
- Li, H., Qiu, Y.F., Wang, X.L., Yang, J., Yu, Y.J., Chen, Y.Q., 2017. Biochar supported Ni/Fe bimetallic nanoparticles to remove 1,1,1-trichloroethane under various reaction conditions. *Chemosphere* 169, 534–541.
- Ling, L.L., Liu, W.J., Zhang, S., Jiang, H., 2017. Magnesium oxide embedded nitrogen self-doped biochar composites: fast and high-efficiency adsorption of heavy metals in an aqueous solution. *Environ. Sci. Technol.* 51, 10081–10089.
- Lobo, F.L., Wang, H., Huggins, T., Rosenblum, J., Linden, K.G., Ren, Z.J., 2016. Low-energy hydraulic fracturing wastewater treatment via AC powered electrocoagulation with biochar. *J. Hazard. Mater.* 309, 180–184.
- Mohan, D., Singh, P., Sarswat, A., Steele, P.H., Pittman Jr., C.U., 2015. Lead sorptive removal using magnetic and nonmagnetic fast pyrolysis energy cane biochars. *J. Colloid Interface Sci.* 448, 238–250.
- Niazi, N.K., Bibi, I., Shahid, M., Ok, Y.S., Burton, E.D., Wang, H., Shaheen, S.M., Rinklebe, J., Lüttge, A., 2018. Arsenic removal by perilla leaf biochar in aqueous solutions and groundwater: an integrated spectroscopic and microscopic examination. *Environ. Pollut.* 232, 31–41.
- Oh, S.Y., Seo, Y.D., Ryu, K.S., 2016. Reductive removal of 2,4-dinitrotoluene and 2,4-dichlorophenol with zero-valent iron-included biochar. *Bioresour. Technol.* 216, 1014–1021.
- Pi, L., Jiang, R., Zhou, W., Zhu, H., Xiao, W., Wang, D., Mao, X., 2015. G-C₃N₄ modified biochar as an adsorptive and photocatalytic material for decontamination of aqueous organic pollutants. *Appl. Surf. Sci.* 358, 231–239.
- Qian, L., Zhang, W., Yan, J., Han, L., Chen, Y., Ouyang, D., Chen, M., 2017. Nanoscale zero-valent iron supported by biochars produced at different temperatures: synthesis mechanism and effect on Cr (VI) removal. *Environ. Pollut.* 223, 153–160.
- Qiu, H., Zhang, S., Pan, B., Zhang, W., Lv, L., 2012. Effect of sulfate on Cu (II) sorption to polymer-supported nano-iron oxides: behavior and XPS study. *J. Colloid Interface Sci.* 366, 37–43.
- Rajapaksha, A.U., Chen, S.S., Tsang, D.C.W., Zhang, M., Vithanage, M., Mandal, S., Gao, B., Bolan, N.S., Ok, Y.S., 2016. Engineered/designer biochar for contaminant removal/immobilization from soil and water: potential and implication of biochar modification. *Chemosphere* 148, 276–291.
- Rajapaksha, A.U., Alam, M.S., Chen, N., Alessi, D.S., Igalavithana, A.D., Tsang, D.C.W., Ok, Y.S., 2018. Removal of hexavalent chromium in aqueous solutions using biochar: chemical and spectroscopic investigations. *Sci. Total Environ.* 625, 1567–1573.
- Rawal, A., Joseph, S.D., Hook, J.M., Chia, C.H., Munroe, P.R., Donne, S., Lin, Y., Phelan, D., Mitchell, D.R., Pace, B., Horvat, J., Webber, J.B.W., 2016. Mineral-biochar composites: molecular structure and porosity. *Environ. Sci. Technol.* 50, 7706–7714.
- Shaffer, D.L., Arias Chavez, L.H., Ben-Sasson, M., Romero-Vargas Castrillón, S., Yip, N.Y., Elimelech, M., 2013. Desalination and reuse of high-salinity shale gas produced water: drivers, technologies, and future directions. *Environ. Sci. Technol.* 47, 9569–9583.
- Shen, Y., 2015. Carbothermal synthesis of metal-functionalized nanostructures for energy and environmental applications. *J. Mater. Chem. A* 3, 13114–13188.
- Shih, J.S., Saiers, J.E., Anisfeld, S.C., Chu, Z., Muehlenbachs, L.A., Olmstead, S.M., 2015. Characterization and analysis of liquid waste from Marcellus Shale gas development. *Environ. Sci. Technol.* 49, 9557–9565.
- Shrestha, N., Chilkoo, G., Wilder, J., Ren, Z.J., Gadhamshetty, V., 2018. Comparative performances of microbial capacitive deionization cell and microbial fuel cell fed with produced water from the Bakken shale. *Bioelectrochemistry* 121, 56–64.
- Stefaniuk, M., Oleszczuk, P., Ok, Y.S., 2016. Review on nano zerovalent iron (nZVI): from synthesis to environmental applications. *Chem. Eng. J.* 287, 618–632.
- Sun, Y.Q., Chen, S.S., Tsang, D.C.W., Graham, N.J.D., Ok, Y.S., Feng, Y.J., Li, X.D., 2017a. Zero-valent iron for the abatement of arsenate and selenate from flowback water of hydraulic fracturing. *Chemosphere* 167, 163–170.
- Sun, Y.Q., Lei, C., Khan, E., Chen, S.S., Tsang, D.C.W., Ok, Y.S., Lin, D.H., Feng, Y.J., Li, X.D., 2017b. Nanoscale zero-valent iron for metal/metalloid removal from model hydraulic fracturing wastewater. *Chemosphere* 176, 315–323.
- Sun, Y.Q., Lei, C., Khan, E., Chen, S.S., Tsang, D.C.W., Ok, Y.S., Lin, D.H., Feng, Y.J., Li, X.D., 2018. Aging effects on chemical transformation and metal(loid) removal by entrapped nanoscale zero-valent iron for hydraulic fracturing wastewater treatment. *Sci. Total Environ.* 615, 498–507.

- Tang, L., Feng, H., Tang, J., Zeng, G., Deng, Y., Wang, J., Liu, Y., Zhou, Y., 2017. Treatment of arsenic in acid wastewater and river sediment by Fe@Fe₂O₃ nanobunches: the effect of environmental conditions and reaction mechanism. *Water Res.* 117, 175–186.
- Wang, S., Gao, B., Li, Y., Wan, Y., Creamer, A.E., 2015. Sorption of arsenate onto magnetic iron-manganese (Fe–Mn) biochar composites. *RSC Adv.* 5, 67971–67978.
- Wang, X., Du, Y., Ma, J., 2016. Novel synthesis of carbon spheres supported nanoscale zero-valent iron for removal of metronidazole. *Appl. Surf. Sci.* 390, 50–59.
- Wang, S., Gao, B., Li, Y., Creamer, A.E., He, F., 2017a. Adsorptive removal of arsenate from aqueous solutions by biochar supported zero-valent iron nanocomposite: batch and continuous flow tests. *J. Hazard. Mater.* 322, 172–181.
- Wang, X., Zhan, C., Ding, Y., Ding, B., Xu, Y., Liu, S., Dong, H., 2017b. Dual-core Fe₂O₃@carbon structure derived from hydrothermal carbonization of chitosan as a highly efficient material for selective adsorption. *ACS Sustain. Chem. Eng.* 5, 1457–1467.
- Wu, M., Ma, J., Cai, Z., Tian, G., Yang, S., Wang, Y., 2015. Rational synthesis of zerovalent iron/bamboo charcoal composites with high saturation magnetization. *RSC Adv.* 5, 88703–88709.
- Yan, Q., Wan, C., Liu, J., Gao, J., Yu, F., Zhang, J., Cai, Z., 2013. Iron nanoparticles in situ encapsulated in biochar-based carbon as an effective catalyst for the conversion of biomass-derived syngas to liquid hydrocarbons. *Green Chem.* 15, 1631–1640.
- Yan, J., Han, L., Gao, W., Xue, S., Chen, M., 2015. Biochar supported nanoscale zerovalent iron composite used as persulfate activator for removing trichloroethylene. *Bioresour. Technol.* 175, 269–274.
- Yang, F., Zhao, L., Gao, B., Xu, X., Cao, X., 2016. The interfacial behavior between biochar and soil minerals and its effect on biochar stability. *Environ. Sci. Technol.* 50, 2264–2271.
- Zhang, Y., Fan, J., Fu, M., Ok, Y.S., Hou, Y., Cai, C., 2017. Adsorption antagonism and synergy of arsenate (V) and cadmium (II) onto Fe-modified rice straw biochars. *Environ. Geochem. Health* 1–12.
- Zhou, Y., Gao, B., Zimmerman, A.R., Cao, X., 2014. Biochar-supported zerovalent iron reclaims silver from aqueous solution to form antimicrobial nanocomposite. *Chemosphere* 117, 801–805.
- Zhu, S., Ho, S.H., Huang, X., Wang, D., Yang, F., Wang, L., Wang, C.Y., Cao, X.D., Ma, F., 2017. Magnetic nanoscale zerovalent iron assisted biochar: interfacial chemical behaviors and heavy metals remediation performance. *ACS Sustain. Chem. Eng.* 5, 9673–9682.